Pharm Res (2014) 31:1710–1723
DOI 10.1007/s11095-013-1274-2

RESEARCH PAPER

Assessment of Physical Stability of an Antibody Drug Conjugate by Higher Order Structure Analysis: Impact of Thiol- Maleimide Chemistry

Jianxin Guo • Sandeep Kumar • Amarnauth Prashad • Jason Starkey • Satish K. Singh

Received: 18 September 2013 / Accepted: 19 December 2013 / Published online: 24 January 2014

ABSTRACT

Purpose To provide a systematic biophysical approach towards a better understanding of impact of conjugation chemistry on higher order structure and physical stability of an antibody drug conjugate (ADC).

Methods ADC was prepared using thiol-maleimide chemistry. Physical stabilities of ADC and its parent IgG1 mAb were compared using calorimetric, spectroscopic and molecular modeling techniques.

Results ADC and mAb respond differently to thermal stress. Both the melting temperatures and heat capacities are substantially lower for the ADC. Spectroscopic experiments show that ADC and mAb have similar secondary and tertiary structures, but these are more easily destabilized by thermal stress on the ADC indicating reduced conformational stability. Molecular modeling calculations suggest a substantial decrease in the conformational energy of the mAb upon conjugation. The local surface around the conjugation sites also becomes more hydrophobic in the ADC, explaining the lower colloidal stability and greater tendency of the ADC to aggregate.

Conclusions Computational and biophysical analyses of an ADC and its parent mAb have provided insights into impact of conjugation on physical stability and pinpointed reasons behind lower structural stability and increased aggregation propensity of the ADC. This knowledge can be used to design appropriate formulations to stabilize the ADC.

KEY WORDS antibody drug conjugates · fluorescent dyes · molecular model · physical stability · thiol-maleimide chemistry

ABBREVIATIONS

ADC	Antibody drug conjugate
ANS	8-Anilino-1-naphthalenesulfonic acid
CD	Circular dichroism
DAR	Drug: antibody ratio
DCVJ	4-(dicyanovinyl)Julolidine
DMSO	Dimethyl sulfoxide
DSC	Differential scanning calorimetry
DSF	Differential scanning fluorimetry
Fab	Fragment antigen binding
Fc	Fragment crystallizable
HC	Heavy chain
LC	Light chain
LP	Linker plus payload
mAb	Monoclonal antibody
OD	Optical density
PDB	Protein Data Bank
RMSD	Root mean square deviation

INTRODUCTION

Antibody-drug conjugates (ADCs) are a class of immunoconjugates that are designed to selectively deliver a

Electronic supplementary material The online version of this article (doi:10.1007/s11095-013-1274-2) contains supplementary material, which is available to authorized users.

J. Guo • S. Kumar • S. K. Singh (✉)
Biotherapeutics Pharmaceutical Sciences, Pharmaceutical R&D, Pfizer Inc.
700 Chesterfield Parkway West, Chesterfield, MO 63017, USA
e-mail: satish.singh@pfizer.com

A. Prashad
Biotherapeutics Pharmaceutical Sciences, Bioprocess R&D, Pfizer Inc.
401 N Middletown Rd, Pearl River, NY 10965, USA

J. Starkey
Biotherapeutics Pharmaceutical Sciences, Analytical R&D, Pfizer Inc.
700 Chesterfield Parkway West, Chesterfield, MO 63017, USA

cytotoxic drug to tumor cells. ADCs are constructed from three components: 1) a mAb that is specific to a cell-surface tumor antigen that is capable of internalization, 2) a highly potent cytotoxic drug aka payload, and 3) a linker that enables covalent attachment of the cytotoxic drug to the mAb (1,2). The chemistry used to link the antibody and the cytotoxic drug is critical to the success of this construct (1,3). Lysine and cysteine are the two most commonly used amino acid residues to conjugate a cytotoxic small molecule drug to the antibody (4–7). For example, Mylotarg® (gemtuzumab ozogamicin) utilizes the acid-labile hydrazone linker to covalently attach calicheamicin to the lysine residues of an anti-CD33 mAb. Adcetris® (brentuximab vedotin) is an ADC formed by thiol-maleimide chemistry, where inter-chain disulfides in an anti-CD30 monoclonal antibody are partially reduced, followed by alkylation with the drug-linker moiety monomethyl auristatin E. Kadcyla® (ado-trastuzumab emtansine, also referred to as trastuzumab-DM1) consists of the therapeutic anti-HER2 monoclonal antibody trastuzumab covalently linked to the maytansine analog DM1 *via* a two-step linkage, which involves lysine conjugation of mAb to linker followed by maleimide chemistry of drug to linker.

By combining the advantages of cytotoxic drugs and monoclonal antibodies (mAbs), ADCs offer unrivaled potential for targeted cancer treatment. However, development of these therapeutic candidates can be challenging due to the heterogeneity of ADC molecules created from the conjugation process (7). Furthermore, for any given ADC, the physicochemical properties of the cytotoxic drug (payload) and linker, combined with selection of linkage site(s), have the ability to impact the conformational and colloidal stability of the conjugated mAb. For example, intra- and inter-molecular interactions, including apolar and electrostatic effects might be altered by the neutralization of the surface charge on the lysine residues that are modified and conjugated. Cleavage of inter-chain disulfide bonds during thiol-maleimide chemistry- based conjugation might lower conformational stability of the mAb molecule (8,9). The addition of linker and drug moieties during processing, as well as the hydrophobicity of the drug itself, might lead to structural changes in the mAb that may affect the stability profile of the conjugated molecule. Despite the advances in ADC technology, it is not well understood how conjugation chemistry, process of conjugation, site of conjugation, and physico-chemical properties of linker and payload affect the overall higher order structure and therefore the physical stability and integrity of the ADCs.

In this study, a model ADC was prepared *via* thiol-maleimide chemistry. The conjugation process involves partial reduction of inter-chain disulfide bonds in an IgG1 mAb and addition of a small molecule that consists of an maleimidocaproyl (mc) linker and an auristatin payload (LP). In order to compare physical stability of the ADC with respect to its parent mAb, both molecules were evaluated by a battery of spectroscopic and calorimetric techniques that provided insights into the types of higher-order structures formed by the ADC and the parent mAb. The aggregation propensities and types of aggregates formed were assessed by intrinsic as well as extrinsic fluorescence spectroscopy and turbidity measurements. Furthermore, a molecular model of full length parent mAb was built *via* homology modeling and was used to create a model for ADC at a drug: antibody ratio (DAR) of four. Molecular mechanics calculations on models of the parent mAb, ADC as well as intermediate structures were performed to assess the impact of disulfide bond breakage and conjugation on conformational stability. It was noted that the conformational stability of the ADC is significantly reduced as compared to the parent mAb with inter-chain disulfide bonds either intact or broken. The local surface around the conjugation sites also becomes more hydrophobic in the ADC. These observations from molecular modeling correlate well with the biophysical experiments that show significant difference between how the ADC and its parent mAb respond to thermal stress. Both the melting temperatures (Tm) and heat capacities measured by differential scanning calorimetry (DSC) are substantially lower for the ADC. The secondary and tertiary structures in the ADC are also more easily destabilized by thermal stress and the ADC is more aggregation prone than its parent mAb. The understanding gained by this study can help devise appropriate formulation strategies to stabilize ADCs and facilitate their development into marketed drug products.

MATERIALS AND METHODS

Materials

The IgG1 parent mAb and the ADC (thiol-maleimide chemistry with mc-auristatin as linker-payload; DAR ranging between 2 and 8) used in this study were produced by Bioprocess R&D at Pfizer Inc. (Pearl River, NY). For most of the assays, both the mAb and the ADC were diluted with 20 mM histidine buffer to a concentration of approximately 0.5 mg/mL. Since histidine displays high absorbance in the far-UV region, mAb and ADC were diluted with water to approximately 0.4 mg/mL for the CD measurements. The final concentrations were determined by UV spectroscopy and used in subsequent analyses. USP/Ph.Eur. grade L-histidine was purchased from JTBaker (Phillipsburg, NJ). Analytical grade ANS (8-Anilino-1-naphthalenesulfonic acid), and thioflavin T were purchased from Sigma-Aldrich Chemical Co. (St. Louis, MO). The SYPRO Orange dye, supplied as a 5000× concentrated solution in dimethyl sulfoxide (DMSO) and 4-(dicyanovinyl)Julolidine (DCVJ) powder were purchased from Invitrogen, Inc. (Carlsbad, CA).

Free auristatin has a very low aqueous solubility (LogS = −7.062; calculated using MOE by CCG, Montreal, Canada). The free auristatin level in the ADC solution is below detection limit (<0.4% wt/wt, free payload over total). It is not expected that free auristatin, even if present at this level, would have any impact on the behavior of intact antibody, Therefore, negative control experiments to deconvolute the interaction (impact) of free auristatin and mAb from the conjugate in the thermal or spectroscopic analyses, were not performed.

Differential Scanning Calorimetry (DSC)

DSC was performed using a high throughput MicroCal VPDSC with autosampler (MicroCal, LLC, Northampton, MA). Thermograms of the mAb and ADC solutions were obtained from 10 to 95°C using a scan rate of 60°C/h. The filled cells were equilibrated for 15 min at 10°C before beginning each scan. Thermograms of the buffer control were subtracted from each mAb or ADC scan prior to analysis. For experiments designed to evaluate the reversibility of the melting transitions, samples were scanned twice at the rate of 60°C/h in the temperature range 10–72°C. Data was processed with Origin 7.0 software (OriginLab; Northampton, MA).

Circular Dichroism

Circular Dichroism (CD) analysis of the antibody and ADC was performed using Chirascan (Applied Photophysics Ltd, UK). Individual CD spectrum was collected from 190 to 320 nm with a 0.1 cm path length cuvette at the beginning of thermal melt (20°C). An optimized sampling time of 6 s, step size of 0.5 nm, bandwidth of 1 nm were used. Note that near- and far-UV CD measurements are traditionally performed separately since the aromatic CD signals are much weaker compared to the peptide-sensitive far-UV region. Typical cell path lengths used for far-UV CD measurements are in the range 0.01–0.1 cm with protein concentrations between 0.1 and 1 mg/mL. In contrast, the near-UV region requires a typical path length of 0.5–2 cm and protein concentrations of 0.5–2.0 mg/mL. However, by following Dr. Middaugh's protocol (10), we were able to collect both near- and far-UV CD measurements simultaneously by optimizing the cell path length, protein concentration and instrument parameter settings.

In the "Results" section, the spectra are presented after subtracting the buffer spectrum as the reference. The CD signal at 218 nm was monitored as a function of temperature to detect heat-induced conformational change of the protein. Samples were heated from 20 to 90°C at 60°C/hr and CD signals were recorded every 1°C. The resulting data were converted from mdeg to molar ellipticity and are plotted as a function of wavelength or temperature.

Intrinsic Fluorescence Spectroscopy

Intrinsic fluorescence spectra were obtained with Varian Cary Eclipse Fluorescence Spectrophotometer (Palo Alto, CA). The mAb and ADC were excited at 295 nm and the emission spectra were recorded from 300 to 400 nm with a resolution of 1 nm. Both the excitation and emission slits were set at 5 nm. Buffer spectra were collected and subtracted from the sample scan. Melt spectra were recorded from 12 to 90°C at 3°C intervals. The wavelength position of maximum emission was determined using a polynomial derivative fitting method executed in the Origin 7.0 software.

ANS Fluorescence Spectroscopy

1-anilino-8-naphthalene sulfonate (ANS) fluorescence spectroscopy was conducted to examine the surface polarity of the antibody and ADC employing the commonly used fluorescent dye ANS (11–13). The fluorescence emission spectra of samples prepared with approximately 80 μM of ANS, were collected from 390 to 600 nm after excitation at 372 nm. While measuring ANS fluorescence, the excitation and emission slit widths were both set to 5 nm. The weak emission spectrum of ANS in buffer was subtracted from the sample spectrum. Melt spectra were again recorded from 12 to 90°C at 3°C intervals. The emission maximum was determined by polynomial derivative fitting method executed in the Origin 7.0 software.

Derivative UV Absorbance Spectroscopy

An Agilent 8,453 diode array UV- Vis spectrometer (Palo Alto, CA) was employed to study UV absorbance temperature perturbation. Spectra were collected every 3°C from 25°C to 90°C with equilibrium time of 1 min at each temperature. A 1 cm cuvette sealed with Teflon stopper (sample volume of 100 μL) was used. Agilent Chem-Station was used to analyze the spectra and second-derivative was acquired using a nine-point data filter, fifth-degree Savitzky-Golay polynomial and were subsequently fitted to a cubic function with 99 interpolated points per raw data point, permitting 0.01 resolution. Optical density (OD) at 350 nm was recorded simultaneously (11,14).

Differential Scanning Fluorimetry (DSF)

Three dyes, namely, Sypro Orange, DCVJ and Thioflavin T were used in DSF experiments to monitor thermal unfolding and formation of aggregates.

Sypro Orange dye was supplied in 5,000-fold concentrated stock solutions. The dye was diluted 2,000-fold in the assay samples. With excitation at 560–590 nm, the fluorescence emission was collected using a ROX filter (600–630 nm).

Both DCVJ and Thioflavin T stock solutions (4 mM) were prepared in DMSO. Prior to use, the stock solutions were diluted 2,000 fold to 20 μM in the assay samples. After excitation at 450–490 nm, the fluorescence emission was collected using a FAM filter (515–530 nm).

The mAb and ADC solutions were prepared in BioRad multiplate® PCR plate. Each cell was filled with 25 μL of sample solution. The plate was sealed with optically clear adhesive PCR Microseal® 'B' film. The fluorescence was monitored by Bio-Rad CFX Real-Time System, C1000 Thermal Cycler. The above plate, plate sealer and plate reader were purchased from BioRad Laboratories (Hercules, CA). The sample plates were subject to thermal stress from 5 to 95°C at an increment of 1°C. At each temperature, the plate was equilibrated for 1 min prior to measurement. The fluorescence data and the second derivatives obtained from the built-in software were exported as CSV file into Microsoft Excel (Microsoft Corporation, Redmond, WA) for further data analysis.

Thermal Incubation and Analytical Size-Exclusion Chromatography

The mAb and ADC (0.5 mg/mL) were incubated at 75°C for 30 min, followed by placing the sample tubes in the ice water mixture to quench the process, and then analyzed by SE-HPLC to quantitate the amount of aggregates formed as well as monomer species. SE-HPLC was performed using an Agilent 1,200 HPLC system (Agilent Technologies, Santa Clara, CA) equipped with a UV detector, an auto-sampler maintained at 4°C, and a temperature controlled column compartment at 25°C.

Samples (20 μL) were injected onto a TSKG3000SWxl (Tosoh Bioscience LLC 7.8 mm ID × 30 cm) column and eluted isocratically over 40 min at a flow rate of 0.75 mL/min. The mobile phase consisted of 20 mM sodium phosphate, 400 mM sodium chloride at pH 7.0. The detection wavelength was set at 280 nm. All species eluting prior to the main peak were integrated together and are reported as high molecular mass species (HMMS).

Molecular Model building for the full length IgG1 mAb

A molecular model for the full length IgG1 mAb was made in two stages. First, a model for just the variable portion (Fv) of the antibody was built using Antibody modeler tool in MOE software package available for Chemical Computing Group (www.chemcomp.com). The Fv model was then superimposed on the Fv portion in the crystal structure of human B12 antibody (15) available from the Protein Data Bank (PDB) (www.rcsb.org, (16)) to construct a chimeric template that was then used to build full length model of the IgG1 mAb *via* homology modeling. The homology modeling process for the IgG1 mAb consisted of creation of one thousand (100 backbone models and 10 side chain models per backbone models) intermediate models which were ranked *via* Generalized Born/Volume Integral (GB/VI) solvation energy. The final model obtained was checked for stereo-chemical quality and was further optimized *via* multiple step energy minimizations. AMBER99 force-field with Reaction field implicit solvation model were used during homology modeling for optimization of intermediate and final models. The values for internal and external dielectric constants were 4 and 80. The non-bonded cut-off distances were set to 10 Å and 12 Å. The final optimized model for full length IgG1 mAb was analyzed for potential physico-chemical vulnerabilities and was taken further for building the models for the ADC.

To understand the impact of disulfide breakage on conformational stability of the IgG1 mAb, the inter-chain disulfide bonds between the light and heavy chains (LC:214 – C222: HC) and those between the heavy chains (HC:C228 – C228:HC, HC: C231 – C231:HC, hinge region) were broken manually and the antibody model was optimized again *via* energy minimizations. The models of IgG1 mAb with inter-chain disulfide bonds either intact or broken were compared for inter-sulfur atom distances and solvent exposure of the Cys residues.

Model Building of ADC

Based on results from mass spectrometric analysis of the ADCs (not shown), the Cys residues that form LC:214 – C222: HC disulfide bonds in the heavy and light chain pairs of the IgG1 mAb were used to develop models of antibody-drug conjugate (ADC). Four LP (mc linker plus auristatin payload) molecules were conjugated to the IgG1 mAb at Cys 214 in both light chains and at Cys 222 in both heavy chains, after breaking the disulfide bonds LC:C214 –C222:HC in both light and heavy chain pairs. This was done by first building in the mc linkers at each of the four Cys residues and optimizing them within the structural context of the mAb, using the builder and energy minimization tools available in MOE. Once the linkers were placed at each site, the auristatin drug payloads were manually attached to the linkers one by one and the overall orientations of the linker and payload were optimized again. The overall structure of the ADC was also optimized *via* energy minimizations. The energy minimizations of the ADC model were carried out using PFROSST force-field available in MOE2012.10. This force-field combines AMBER parameters for proteins with parm@Frosst parameters for small molecules. Further information on this force-field can be found in help pages of MOE.

The final energy minimized model of the ADC was further subjected to conformational searches for the four LP molecules, the four conjugated Cys residues and the nearby residues (4.5 Å). Four significantly different low energy ADC

conformers were obtained. Each of these ADC conformers was further optimized by subjecting them to all-atom energy minimizations.

RESULTS

Thermal Analysis

The results of overall structural stability as assessed by DSC shows that the ADC has lower thermal stability compared to the parent mAb. Both molecules were analyzed in solutions containing the same buffer components at 0.5 mg/mL. The DSC thermograms for both the parent mAb and the ADC, show two transitions (Fig. 1a). The melting temperatures associated with these transitions are higher for the parent mAb ($T_{m1}=68.6°C$ and $T_{m2}=83.2°C$) than the ADC ($T_{m1}=66.3°C$ and $T_{m2}=80.5°C$). The decrease in melting temperatures is also accompanied by lower heat capacities (Cp) for both the transitions in case of the ADC. The Cps for the ADC are almost half of that for the corresponding transitions of the parent mAb (Fig. 1a). The width of the first transition is 4.5°C (temperature width at half peak-height) for both ADC and mAb, but the second transition is much wider for the ADC (7.8°C) compared to mAb (4.3°C) (Fig. 1a).

The reversibility of the first transition in the two molecules was also evaluated. This calorimetric reversibility typically indicates that the transition from the native to the unfolded state is reversible and that the unfolded state will return to the native state upon cooling. For testing reversibility, the samples were rescanned following the initial sample scan in the temperature range ~10–72°C. The trace of the DSC thermograms for the initial sample scan and the subsequent rescan were assessed for superimposability, as shown in Fig. 1b. On the basis of our results, the first DSC transition for the mAb is reversible with 100% enthalpy recovery, while for the ADC, it is partially reversible with 65% enthalpy recovery.

Secondary Structure

Structure assessed by far-UV CD (190–250 nm) shows that ADC and mAb have similar secondary structures, but this is more easily destabilized on the ADC under thermal stress. Both the mAb and ADC show a prominent minimum at 218 nm, indicative of ß-sheet dominant antibody characteristics. No significant difference in secondary structure was found between the mAb and ADC at 20°C (Fig. 2a). In addition to acquiring full-length spectra, we monitored the intensity of the minimum at 218 nm as a function of temperature from 20 to 90°C in 3°C increments (Fig. 2b). By thermally stressing the protein in this manner, we can ascertain the relative stability of the secondary structure. At elevated temperatures, the molar ellipticity decreases (*i.e.*, becomes more negative), suggesting the formation of aggregates (17). There appear to be two transitions (indicated by arrows) in the Fig. 2b. The onsets of both transitions occur at lower temperatures for ADC (~65°C and ~76°C) as compared to mAb (~70°C and ~82°C, respectively). These observations indicate that both ADC and the parent mAb are rich in β-strands. However, the ADC has lower secondary structural stability.

Tertiary Structure

Structure assessed by near-UV CD (250–320 nm) shows that the ADC and mAb also share similar tertiary structures. Near-UV CD (250–320 nm) detects the contributions from aromatic side chains. Generally, the CD bands at 262, 266, and 269 nm arise from the phenylalanyl side chains and the band

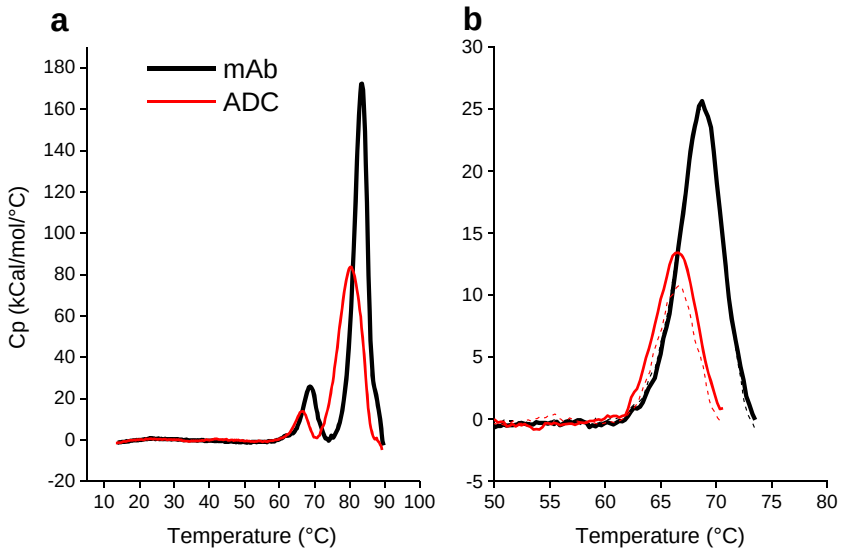

Fig. 1 DSC thermograms of mAb and ADC. The mAb is shown in *bold-black* and ADC in *red*. (**a**) Thermogram over temperature ranges10–90°C. (**b**) Reversibility of the first transition after heating up to 72°C. The first scan is shown as a *solid line* while the second scan is the *dotted line*.

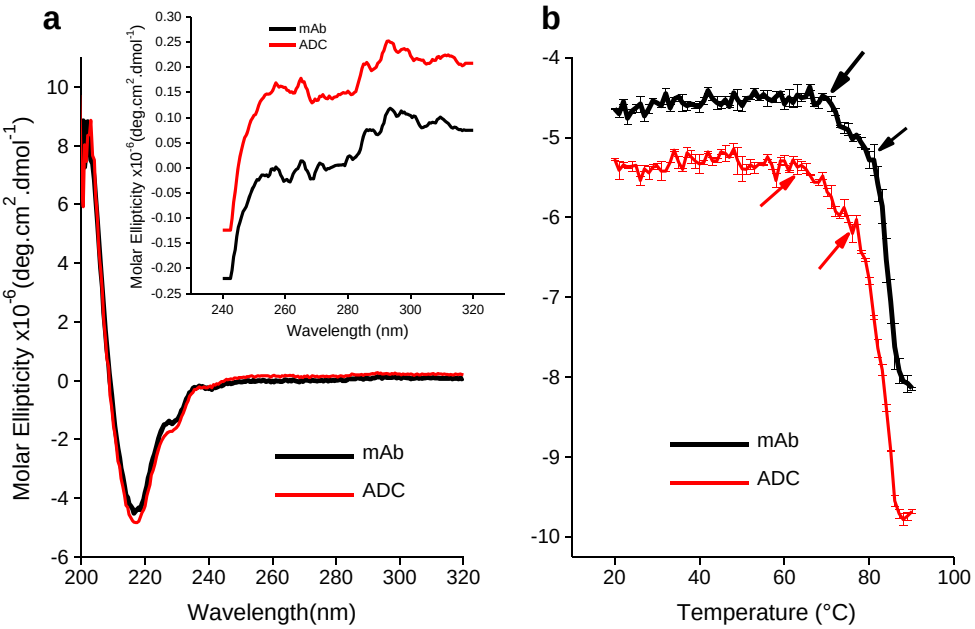

Fig. 2 Circular dichroism measurements of mAb and ADC. The mAb is shown in *bold-black* and ADC in *red*. (**a**) Far-UV + Near-UV CD spectrum (200 to 320 nm). Inset: Expanded view of near-UV CD spectrum (240 to 320 nm). (**b**) Molar ellipticity at 218 nm monitored from 20 to 90°C. Individual data points are the average of three measurements.

near 282 nm from tyrosyl residues. The CD bands at 288 and 289 nm can be attributed to tryptophanyl and/or tyrosyl side chains, while those near 296 nm arise from indolyl groups(18). The near-UV spectra overlap well between mAb and ADC (Fig. 2a). Even after magnification (insert in Fig. 2a), no significant differences were observed (19). This agrees with the intrinsic fluorescence spectra which show a complete overlap between mAb and ADC (Fig. 3a), indicating similar tryptophan environment.

A third technique, second derivative UV absorption spectroscopy, was applied to look for subtle differences in the tertiary structures of the mAb and ADC (Fig. 3b). Second-derivative UV absorbance can permit small changes in tertiary structure to be readily detected when compared to other spectroscopic approaches since the three aromatic residues, phenylalanine, tryptophan and tyrosine, are dispersed throughout the protein primary sequence (20,21). Six distinct negative peaks, three from phenylalanine (258.0 nm, 265.0 nm, and 269.0 nm), and one each from tyrosine (275 nm), tryptophan/tyrosine (284.0 nm) and tryptophan (291.0 nm) were observed in second-derivative UV absorbance spectra of mAb. For ADC, the peaks are at similar positions with minor variations (Fig. 3b).

Tertiary structure stability was evaluated by monitoring maximum fluorescence intensity and peak position as a function of temperature. At the transition temperatures, fluorescence intensity increases (Fig. 3c) and peak position (Fig. 3d) shifts to higher wavelength. There appear to be two transitions (indicated by the arrows) in Fig. 3c. The first transition shows a minor increase in fluorescence intensity at ~65°C for the ADC and ~70°C for mAb. The second transition accompanied by a stronger intensity change is seen at 82°C for ADC and 85°C for intact mAb, These results indicate that the tertiary structure of the ADC has lower stability than that of the mAb. A plot of fluorescence peak position change (Fig. 3d) also shows that the onset of transition occurs at ~65°C for ADC and ~70°C for mAb, corresponding to the first transition observed as change in intensity (Fig. 3c).

Taken together, the results from the spectroscopic analyses consistently show that both the secondary and tertiary structures of the ADC are similar but less stable than the intact mAb. These observations are consistent with results from DSC experiments.

Extrinsic Fluorescence Spectroscopy

Monitoring dye-based extrinsic fluorescence under heating conditions shows that the ADC is more aggregation prone than its parent mAb. The fluorescent dye ANS (8-Anilino-1-naphthalene sulfonic acid) is known to have an affinity for the apolar regions of proteins. As the structure of the protein begins to unfold, the dye partitions into the apolar core, causing an increase in its fluorescence quantum yield (compared to a negligible yield in a polar or aqueous environment). The ADC displays stronger ANS binding intensities compared to the mAb even at low temperatures. Since there is no detectable difference in tertiary structure at these temperatures, it is possible that this intensity difference is due to the presence of the hydrophobic payload leading to non-specific interactions with the dye. On heating above 50°C, temperature-induced ANS binding shows a biphasic response, characteristic for mAb and ADC (Fig. 4a). The onset of binding occurs at approximately 6°C lower temperature for ADC compared to mAb (57°C and 72°C for the ADC

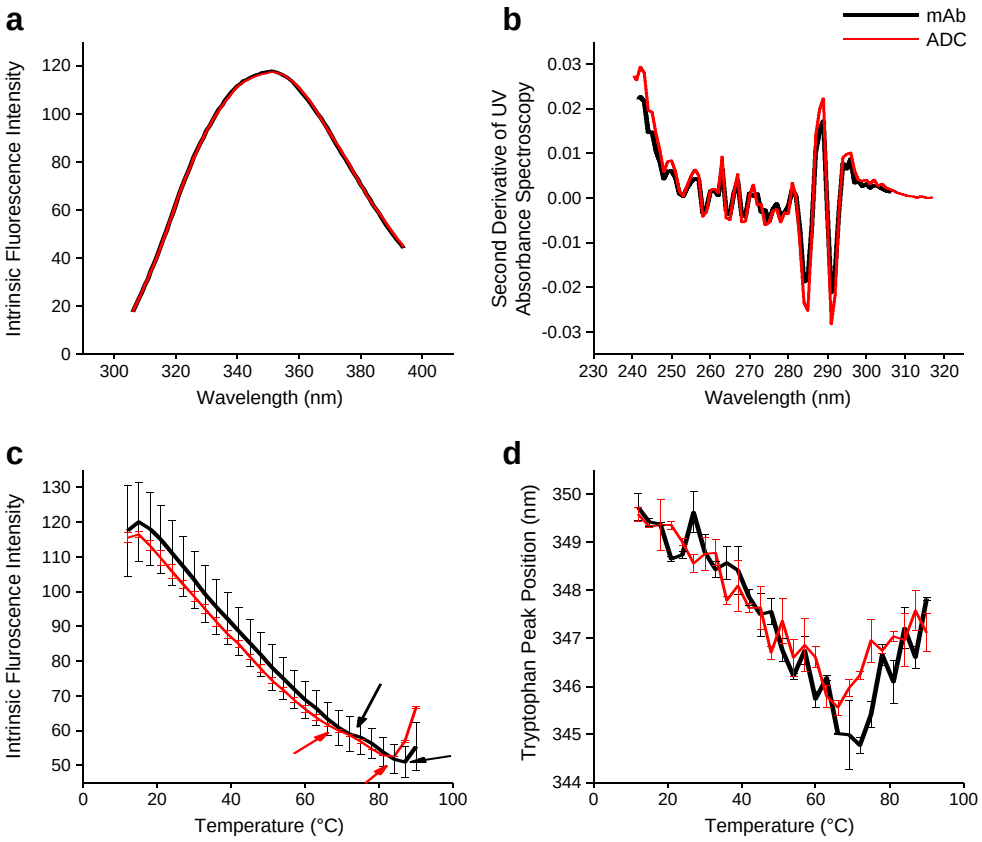

Fig. 3 Spectroscopic analysis of mAb and ADC. The mAb is shown in *bold-black* and ADC in *red*. (**a**) Intrinsic fluorescence spectra for mAb and ADC at 12°C. (**b**) Second derivative UV absorbance spectrum for mAb and ADC at 25°C. (**c**) Maximum fluorescence intensity for mAb and ADC as a function of temperature. (**d**) Fluorescence peak positions for mAb and ADC as a function of temperature.

compared to 63°C and 78°C respectively for the mAb) and the intensity is maintained at a higher level at all temperatures, indicating a more accessible hydrophobic core, post-conjugation (Fig. 4a).

Similar to ANS, Sypro Orange is also an environmentally sensitive fluorescence probe which binds to hydrophobic residues or patches (22). In aqueous solutions, the fluorescence emission from free probes is negligible, but in the presence of unfolded protein, the fluorescence intensity increases significantly due to the increased exposure of the hydrophobic protein interior, which provides hydrophobic regions to which the probe can bind. The utilization of Sypro Orange in the thermal assay is often referred to as differential scanning fluorimetry (DSF).

DSF shows a similar trend to the one observed by ANS fluorescence. Analogous to ANS, more Sypro Orange binds to the ADC compared to the mAb at 5°C. Upon unfolding, a more dramatic increase in fluorescence intensity is observed for the ADC (Fig. 4b). Two temperature-dependent transitions are clearly observed for the mAb and ADC after first derivative treatment of fluorescence intensity profile, indicative of two domains that have different conformational stabilities (Fig. 4c).

DCVJ is one of a class of viscosity-sensitive fluorescent dyes, commonly referred to as molecular rotors (23–25). When DCVJ binds to aggregates, the dye becomes partially immobilized, accompanied by an increase in quantum yield (26,27). Studies have shown that DCVJ responds to the early stages of aggregation and, thus, has a strong preference for oligomeric aggregates (27). Again, similar to ANS and Sypro Orange, DCVJ gives a higher signal at low temperatures for the ADC compared to mAb (Fig. 4d). However, the difference between DCVJ-ADC and DCVJ-mAb is large in the case of DCVJ (compared to ANS and Sypro Orange). In all cases, on heating up to about 55°C, the intensity in the ADC solution decreases. This is most apparent in DCVJ-ADC due to the higher initial value, but the same occurs with the other dyes. We hypothesize that there may be some non-specific and loose hydrophobicity driven interaction of the dyes with the ADC leading to the initial signal, that is simply disrupted by thermal energy on heating. The behavior below ~50–55°C is therefore expected to have no structural implications.

On heating the solution beyond ~55°C, DCVJ intensity increases and reveals two transitions for the ADC (Fig. 4d) more clearly evident in the derivative plot (Fig. 4e). The two transitions are coincident with the conformational changes detected by DSC and DSF. On the other hand, no DCVJ intensity change was observed with the mAb at elevated temperatures in contrast to the response of ANS and Sypro Orange with mAb (compare Fig. 4d with a and b). These results indicate that upon heating under similar experimental conditions the mAb does not aggregate (to detectable levels), while the ADC forms oligomers after unfolding.

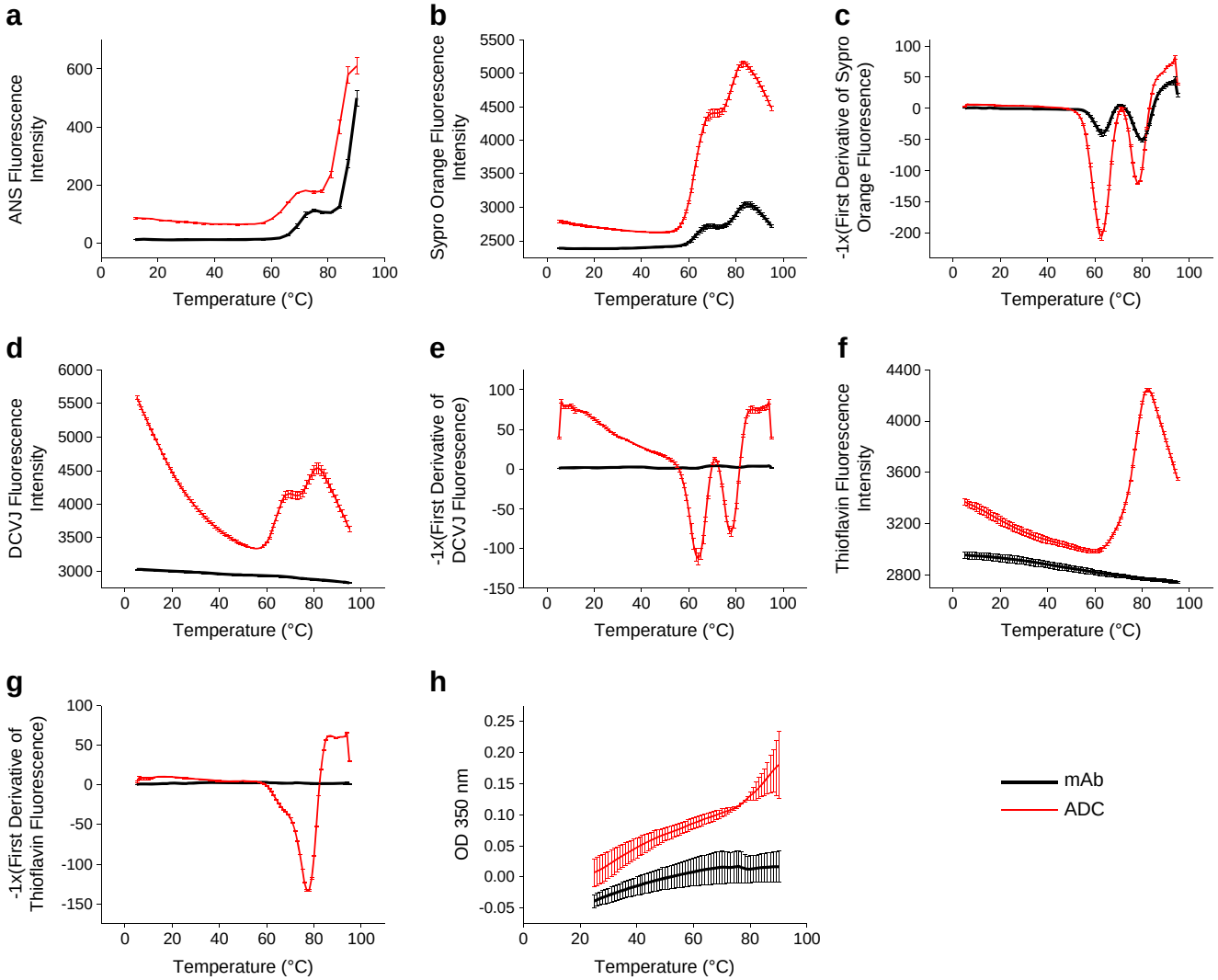

Fig. 4 Extrinsic fluorescence intensity and turbidity profile of mAb and ADC as a function of temperature. The mAb is shown in *bold-black* and ADC in *red*. (**a**) ANS fluorescence intensity. (**b**) Sypro Orange fluorescence intensity. (**c**) First derivative Sypro Orange fluorescence intensity. (**d**) DCVJ fluorescence intensity. (**e**) First derivative DCVJ fluorescence intensity. (**f**) Thioflavin T fluorescence intensity. (**g**) First derivative Thioflavin T fluorescence intensity. (**h**) Turbidity (OD 350 nm) profile. Note that the First derivatives are plotted as $-I*(dI/dT)$.

The formation of cross-β steric zipper motif (28,29) mediated aggregates that can potentially form amyloid-like fibrils is monitored by means of Thioflavin T fluorescence (12,30). Thioflavin T recognizes certain features of the amyloid-type protein aggregates, *e.g.*, ß-sheets and the surfaces formed by tyrosine residues and between the protofilaments, with non-specific interactions (12). Similar to the other dyes, the low temperature response of Thioflavin T with ADC is higher than with mAb and decreases with increasing temperature below about 55°C. At 0.5 mg/mL concentration, no significant change in Thioflavin T fluorescence intensity upon heating above ~55°C was observed for the IgG1 mAb, indicating that cross-β mediated aggregates are either not formed or are too small to be detected (Fig. 4f and g). Only one major transition was obtained at approximately 77°C for ADC (Fig. 4g) although there was a shoulder at 65°C. This transition detected by Thioflavin T corresponds to the second transition at a higher temperature observed by DSC, Sypro Orange and DCVJ fluorescence.

Turbidity

Turbidity measurement (measured as the OD 350 nm recorded during UV absorption experiments) further demonstrates that ADC is more prone to aggregation. The turbidity of ADC sample at 25°C (Fig. 4h) was higher than that of intact mAb even though the aggregate levels determined by SE-HPLC were similar (2.0% for mAb and 1.3% for ADC). Furthermore there were no aggregates detectable by DLS for either mAb or ADC (data not shown). Therefore, the higher turbidity of the unstressed ADC sample (at 25°C) could be attributed to the conjugation of hydrophobic payloads

causing ADC molecules to have a higher degree of self-association (31). On heating up to 85°C, only a very slight change in OD was detected for the mAb, suggesting no detectable major aggregation event (Fig. 4h). In the case of the ADC, heating results in a steady increase in OD 350 nm, with a significant increase above 75°C. The steady increase in OD is interpreted as an increase in the self-association behavior. The jump in OD above 75°C is indicative of a critical temperature for aggregation. This temperature detected by turbidity measurements agrees with the transition peak detected by Thioflavin T fluorescence and shows correlation with the second transition detected by DSC, Sypro Orange and DCVJ fluorescence.

Aggregation Detected by SE-HPLC

Thermal incubation also provides evidence that the ADC aggregates more rapidly compared to the unconjugated mAb. After incubation at 75°C for 30 mins, high molecular mass species (HMMS) increased from initial 2.0% to 2.4% for the mAb. For the ADC, HMMS increased from initial 1.3% to 36.2% in the stressed sample (Fig. 5). The aggregates appear to be predominantly composed of multimers with a small amount of oligomers.

Summarizing the results from extrinsic fluorescence and SE-HPLC experiments, it appears that the ADC is more susceptible to aggregation than the unconjugated mAb even at dilute concentrations.

Molecular Structure Analysis of IgG1 mAb and ADC

A full length molecular model for IgG1 mAb was made using the procedures described in the "Methods" section. The parent mAb structural model was then used to derive models for IgG1 mAb with inter-light chain-heavy chain disulfide bond broken, with just the four linkers attached to the Cys residues in the upper hinge region that become free upon disulfide bond breakage and the full ADC (DAR = 4) with both linkers and payloads attached to the parent mAb. The following inter-related questions were asked: 1. What is the impact of disulfide bond breakage and thiol conjugation on conformational stability of the mAb? 2. What are the local changes in the environments of the cysteine residues and their neighbors in presence of the payload? 3. Can we separate the impact of Linkers *versus* Payloads on stability of the parent mAb? 4. How does conjugation lead to increased aggregation propensity for the ADC?

Figure S1 in the Supplementary Material shows a full length of model of IgG1 mAb. It consists of two heavy chains, H and K, shown in red and blue colored ribbons, and two light chains, L and M, shown in green and brown colored ribbons. Note that overall mAb quaternary structure is asymmetric due to the conformational differences between the two Heavy chain : Light chain pairs. A consequence of this property of antibody structure is that the solvent exposures of Cys residues involved in the two inter-chain disulfide bonds LC:Cys214—Cys222:HC are different. Their microenvironments are also different (see below). These features may be important considerations towards determining reactivities of different Cys residues towards small molecule linker and payload (LP) conjugates.

As described in the "Methods" section, the two inter-chain disulfide bonds connecting heavy and light chains (H: Cys222—Cys214:L and K:Cys222–Cys214:M) were broken manually and the model of IgG1 mAb with broken disulfide bonds was optimized again *via* energy minimization. The models of IgG1 mAb with intact and broken inter-heavy-light chain disulfide bonds superimpose on each with a C^{α}-atom root mean square deviation (RMSD) value of 2.14 Å. For large molecules such as a full length antibody, this value indicates that there are no large-scale structural changes as a consequence of the breakage of these disulfide bonds. However, there are notable changes in the local structure. The residues neighboring Cys222 in the heavy chain H (H: Ser209 – H: Pro 230) show large movements with their C^{α} atoms deviations being in the range of 2.9 Å–6.6 Å. Similarly, C^{α}-atoms of the residues around Cys214 in the light chain L also show large deviations (>4 Å). Upon breakage of a disulfide bond, the two sulfur atoms move farther away from each other but still remain within 4 Å distance. The sulfur atom distance for the Cys residues that participate the disulfide bond H: Cys222—Cys214:L increases to 3.65 Å after this bond is broken. For the other disulfide bond, K: Cys222—Cys214:M, the sulfur atom distance increases to 3.93 Å. Figure S2 in the Supplementary Material shows a superimposition of IgG1 mAb with inter-chain disulfide bonds intact

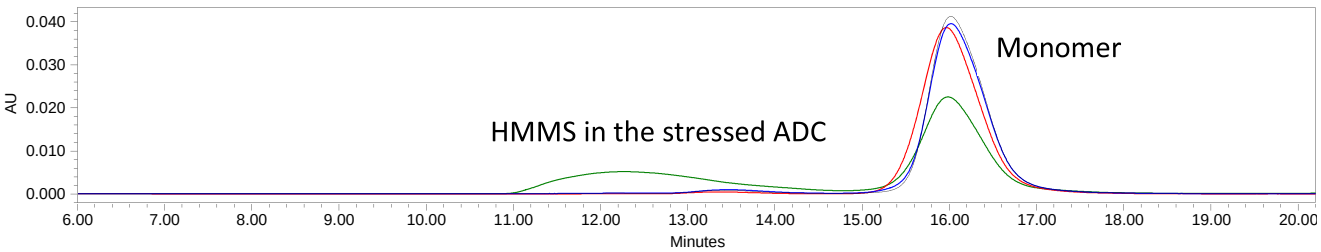

Fig. 5 Overlay of SE-HPLC chromatograms of unstressed mAb (*black*), unstressed ADC (*red*), heat-stressed mAb (*blue*) and heat-stressed ADC (*green*).

and broken. It can be seen that the local conformation of the hinge residues in two heavy chains as well as the conformations of termini regions of the two light chains also change upon breakage of these inter-chain disulfide bonds. Another consequence of breakage of these disulfide bonds is that the solvent exposure of the Cys residues changes and these residues become slightly more solvent exposed. The changes in solvent exposures of these residues are summarized in Table 1.

The four Cys residues freed by breaking the inter-heavy-light chain disulfide bonds were conjugated with four moieties, each consisting of an mc linker and an auristatin payload (LP), to obtain a model of the antibody-drug conjugate (ADC) at DAR of 4. Figure 6 shows a model of the ADC. It can be seen that the four payload moieties occupy the spaces between the two Fabs and the upper hinge region. It is conceivable that the four moieties would move with respect to the mAb structure as well as with respect to one another. To capture, the salient features of this motion, this model of ADC was subjected to conformational search *via* low mode MD simulation module implemented in MOE2012.10 to obtain four additional conformers that show different orientations of LPs within the structural context of the IgG1 mAb. These ADC models, along with those of IgG1 mAb with all disulfide bonds intact, with inter light chain-heavy chain disulfide bonds broken and with just the linkers attached, were analyzed for impact of conjugation on local and global structure of the mAb.

At the local structural level, conjugation with small molecules affects solvent exposure of the Cys residues. Table 1 indicates that solvent exposure of all Cys residues, except K: Cys222, increases significantly upon conjugation. Due to conjugation, the Cys residues which earlier formed inter-heavy-light chain disulfide bonds move further apart from each other. The distance between sulfur atoms of residues H: Cys222 and L: Cys214 increases to 5.36 Å upon conjugation as compared to 3.65 Å when this disulfide bond is broken but the Cys residues are not conjugated. Similarly, the distance between the sulfur atoms of residues K:Cys222 and M: Cys214 becomes 5.18 Å, an increase of 1.25 Å over 3.93 Å distance when the Cys residues are not conjugated.

Table 1 Changes in Solvent Exposure of Heavy Chain Cys222 and Light Chain Cys214 Residues Upon Breakage of Inter-Heavy-Light Chain Disulfide Bonds and Upon Conjugation

Chain: Residue	Disulfide bonds intact ASA (%)	Disulfide bonds broken ASA (%)	Antibody drug conjugate (ADC) ASA (%)
H:Cys222	22.2	26.4	102.3
K:Cys222	0.0	1.8	4.3
L:Cys214	33.0	39.4	80.3
M:Cys214	10.1	15.2	96.4

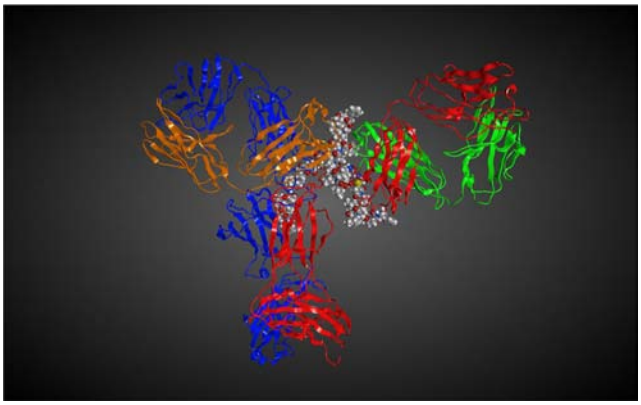

Fig. 6 A molecular model of IgG1 mAb conjugated with four linker-payload moieties. The two light chains are shown in *green* and *brown* ribbons and the two heavy chains are shown in *blue* and *red* colored ribbons. The locations of linker-payload and the Cys residues they are conjugated to, are indicated by showing them in CPK representation.

The global changes in the mAb structure upon conjugation were measured by computing values for C^{α}-atom RMSD, Van der Waals (VdW) volume and polar as well as non-polar surface area (Table 2). Formation of the full ADC leads to significantly greater conformational perturbation in the structure of the parent mAb than either the breakage of inter-light chain-heavy chain disulfide bonds or addition of just the linkers at the four Cys residues in the upper hinge region (Table 2). C^{α} atom RMSDs for ADC model as well as the conformers show an average value of 6.40 ± 0.81 Å when superposed on to the parent IgG1 mAb. In comparison, structural models of the mAb with inter-light chain-heavy chain disulfide bonds broken and with only the linkers attached deviate by only 2.14 Å and 1.76 Å, respectively (Table 2). Figure S3 in the Supplementary Material superposed the ADC model (blue ribbons) on to the model of the parent IgG1 mAb (red ribbons). The superposition suggests that two Fabs and the Fc region move closer to one another in the ADC model due to significant movements in and around the hinge region that appear to facilitate interactions among the four payload moieties.

Conjugation leads to increase in Van der Waals (VdW) volume of the mAb. The VdW volume of the parent IgG1 mAb with all its disulfide bonds intact is 133946.5 $Å^3$. It increases by 93.6 $Å^3$ (~0.07%) when inter light chain-heavy chain disulfide bonds are broken. In contrast, the average volume of the ADC and the four conformers is 134632.6 ± 28.9 $Å^3$, an increase of 686.1 $Å^3$ (~0.5%). A major portion of this increase in the volume of the ADC over the parent IgG1 mAbs is due to the volume of payload molecules themselves. The VdW volume of the parent mAb in the ADC form increases to 134000.6 $Å^3$. Therefore, the payload molecules account for 631.7 $Å^3$ (134632.6 $Å^3$ - 134000.6 $Å^3$ = 631.7 $Å^3$) of the 686.1 $Å^3$ increase in the VdW volume of the ADC. The remainder 54.4 $Å^3$ (686.1 $Å^3$ – 631.7 $Å^3$ = 54.4 $Å^3$, ~8% of the

Table 2 Global Structural Changes in mAb Upon Conjugation

Structural model	Van der Waals volume (Å^3)	Hydrophilic Van der Waals surface area (Å^2)	Hydrophobic Van der Waals surface area (Å^2)	Ratio[a]	C^{α} atom root mean square deviation (Å)
IgG1mAb[b]	133946.5	20521.2	27957.9	1.36	0.0
IgG1 mAb with disulfide bonds broken[b]	134040.1	20474.6	28067.6	1.37	2.139
IgG1mAb with four linkers	134611.9	20337.0	28063.8	1.38	1.762
ADC[b]	134638.2	19756.6	27812.6	1.41	6.088
ADC Conformer 1[b]	134664.9	19787.7	27838.4	1.41	5.993
ADC conformer 2[b]	134634.5	19643.3	27845.7	1.42	5.991
ADC conformer 3[b]	134585.6	19597.7	27927.2	1.42	7.843
ADC conformer 4[b]	134639.6	19755.4	27819.3	1.41	6.092

[a] Ratio, ratio of hydrophobic to hydrophilic Van der Waal's surface area

[b] IgG1mAb, IgG1 mAb with all disulfide bonds intact; IgG1 mAb with disulfide bonds broken, IgG1 mAb with the two inter-heavy-light chain disulfide bonds broken; IgG1 mAb with four linkers, IgG1 mAb with only the linkers (Ls) attached to the four Cys residues freed by breaking the two inter-heavy-light chain disulfide bonds broken; ADC, the full ADC obtained by conjugating four LP molecules to IgG1 mAb; ADC conformers 1,2,3 and 4, the ADC conformers obtained *via* low Mode MD

increased volume) is due to expansion of the parent mAb upon conjugation.

Ratio of hydrophobic to hydrophilic VdW surface area of the ADC *versus* the parent mAb measures the overall shift in composition of the molecular surface upon conjugation (Table 2). Van der Waal's surface becomes more hydrophobic for the ADC as compared to the parent IgG1 mAb. The average value of hydrophobic to hydrophilic surface area ratio for the ADC model and the four conformers is 1.413 ± 0.008. In comparison, the value for this ratio is 1.36 for the parent IgG1 mAb. The changes in hydrophobic and hydrophilic surface areas were further examined to understand how the payload molecules change the surface characteristics of the IgG1 mAb. The total hydrophobic surface area of IgG1 mAb with all inter-chain disulfide bonds intact is 27957.9 Å^2. Upon conjugation, the hydrophobic surface area of the ADC is 27812.6 Å^2 ($\Delta ASA_{np} = -145.3$ Å^2, ~0.5% decrease). The total hydrophilic surface area for IgG1 mAb is 20521.2 Å^2 which decreases to 19756.6 Å^2 ($\Delta ASA_{p} = -764.6$ Å^2, ~3.7% decrease) in the ADC (Table 1). Therefore, the four payload molecules cover mostly the polar surface on the parent mAb. Figure 7(a) and (b) show hydrophilic and hydrophobic surfaces around the location of small molecule moieties in the ADC. The calculated logS (solubility in water) value for auristatin is −7.0672. Conjugation of these extremely low solubility molecules on the mAb surface enhances the overall hydrophobicity of the ADC as compared to the parent mAb.

In summary, the data shown in Table 2 indicate that significant changes occur in the global structure of the mAb upon conjugation. Furthermore, addition of the four auristatin payload molecules contributes significantly more towards these changes than breakage of inter-light chain—heavy chain disulfide bonds or attachment of the four linkers.

Molecular mechanics calculations were used to estimate the destabilization of IgG1 upon breakage of inter-chain disulfide bonds, upon addition of the four linkers and upon full conjugation (linkers plus payloads). These calculations

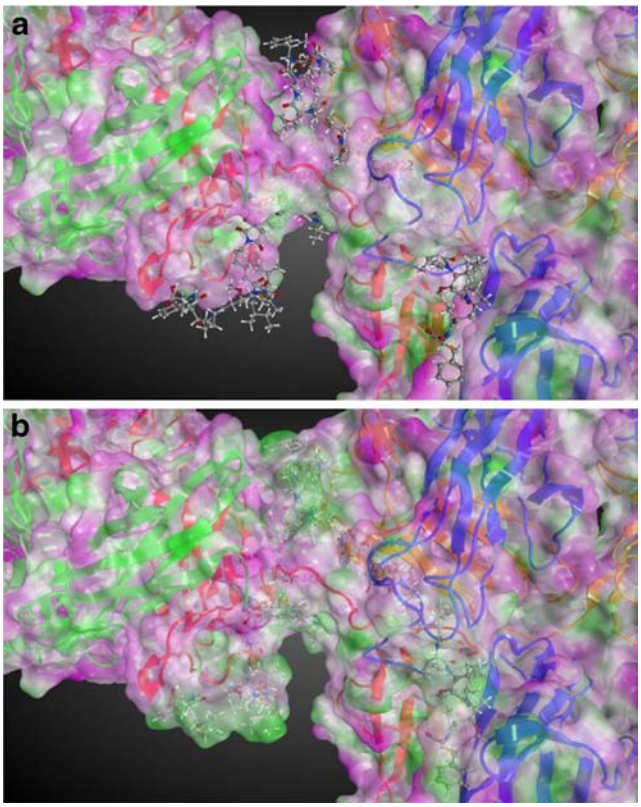

Fig. 7 (**a**) Hydrophilic (*pink*) and hydrophobic (*green*) features on the IgG1 mAb surface around linker-payload (LP) moieties in the ADC. The LPs are shown in ball and stick representation on the IgG1 mAb surface. (**b**) Hydrophilic (*pink*) and hydrophobic (*green*) features on the surface of the ADC (IgG1 mAb plus four LP). The surfaces depicted here include the LP surfaces. By comparing the panels (**a**) and (**b**), it can be seen that local mAb surface becomes more hydrophobic upon conjugation. In both the panels, molecular surface was made transparent to reveal the underlying structural features of the mAb. The features are represented by ribbons that are differently colored for each light and heavy chain of the mAb.

were performed on the various models after minimizing them with PFROSST force-field. Table 3 presents the calculated potential energies of IgG1 mAb with all inter-chain disulfide bonds intact, IgG1 mAb with two inter-heavy-light chains broken, IgG1 mAb with only the four mc linkers attached and, finally, the full ADC with all four payload molecules attached. As expected, breakage of the two inter-chain disulfide bonds leads to destabilization of the mAb and attachment of the mc linkers leads to further destabilization. The full ADC is significantly more destabilized than all other models, indicating that addition of payload auristatin molecules leads to a major destabilization of the ADC (Table 3). This observation agrees well with the data on global structural changes described above (Table 2). Note that the molecular mechanics energy values presented here are for ΔE (change in energy between folded and unfolded state of mAb/ADC) and not ΔΔE (change in energy upon disulfide bond breakage, linker attachment or full conjugation). In this report, the trends in ΔE values matched qualitatively with those shown by the enthalpy (H) and heat capacity (Cp) observed in the DSC experiments (see below). To further explore this finding, the four payload molecules, the conjugated Cys residues and nearby residues in the ADC were subjected to conformational search *via* LowModeMD using the default options in MOE2012.10 (www.chemcomp.com). Four low energy conformers were selected and subjected to further all atom optimizations by energy minimizing them. The potential energies of these conformers are also shown in Table 3. Again, it can be seen that even most stable conformer (conformer 3) is significantly more destabilized as compared to IgG1 mAb, IgG1 mAb with two inter-chain disulfide bonds broken and IgG1 mAb with just the linkers attached. Overall, these results indicate that ADC is significantly more destabilized than the parent mAb, and surprisingly it is the addition of the auristatin payload that contributes the most towards destabilization. The DSC thermograms of ADC also show decreased melting temperatures as well as smaller Cp for both the transitions (see "Thermal Analysis" section). Significantly higher potential energy values observed for the energy minimized ADC and its different low mode MD conformers are consistent with experimental observation that Cp for the ADC is almost half that of the IgG1 mAb in the DSC thermograms.

DISCUSSION

The higher order structure of the ADC and its parent IgG1 mAb were studied. To assess the structural stability, ADC and mAb were subjected to temperature-induced unfolding using DSC. The DSC profile shows two transitions in both cases. Ionescu *et al.* (32) have studied the temperature-induced unfolding of the three humanized IgG1 molecules and their Fab and Fc fragments by DSC. Their studies also included an investigation of the effect of variable domains present in IgG1 on the structural stability of the antibody. On the basis of the measured enthalpy of unfolding, it was proposed that, if the variable domain sequences in the IgG1 do not affect the thermal stability of the Fab fragment, then the first transition in the DSC thermogram represents the melting of the conserved heavy chain2 (C_H2) domain while the second transition represents melting of the C_H3 domain and the Fab fragment. Our results with the IgG1 mAb and ADC were consistent with their observations. The first transition, which has a lower experimental enthalpy, represents the unfolding of the C_H2 domain, while the second transition, with a higher experimental enthalpy, represents melting of the C_H3 domain and the Fab region.

The DSC thermogram indicates that the stability of the various domains is impacted differently by conjugation. A

Table 3 Molecular Mechanics Energy Calculations

Structural model	ΔE_{tot} (Kcal/mol)	ΔE_{str} (Kcal/mol)	ΔE_{ang} (Kcal/mol)	ΔE_{oop} (Kcal/mol)	ΔE_{tor} (Kcal/mol)	ΔE_{vdw} (Kcal/mol)	ΔE_{elec} (Kcal/mol)
IgG1mAb[a]	−607.074	355.022	2061.358	85.899	11517.43	−8504.13	−6122.64
IgG1 mAb with disulfide bonds broken[a]	−599.252	356.129	2057.944	82.844	11502.88	−8452.85	−6146.20
IgG1mAb with four linkers	−596.506	358.724	2100.127	83.165	11567.80	−8531.98	−6174.34
ADC[a]	−320.796	395.099	2271.185	88.747	11877.22	−8749.99	−6203.05
ADC conformer 1[a]	−422.073	389.556	2229.320	87.158	11869.04	−8791.87	−6205.27
ADC conformer 2[a]	−397.396	391.299	2261.951	88.513	11862.56	−8802.74	−6198.97
ADC conformer 3[a]	−463.303	387.721	2235.417	85.856	11849.43	−8829.48	−6192.23
ADC conformer 4[a]	−320.804	395.126	2271.255	88.717	11877.01	−8749.89	−6203.02

[a] IgG1mAb, IgG1 mAb with all inter-chain disulfide bonds intact; IgG1 mAb with disulfide bonds broken, IgG1 mAb with the two inter-heavy-light chain disulfide bonds broken; IgG1 mAb with four linkers, IgG1 mAb with only the linkers (Ls) attached to the four Cys residues freed by breaking the two inter-heavy-light chain disulfide bonds broken; ADC, the full ADC obtained by conjugating four LP molecules to IgG1 mAb; ADC conformers 1,2,3 and 4, the ADC conformers obtained *via* low Mode MD. Note that these are ΔE values and not ΔΔE values

decrease in Tm for both the first and second transition following conjugation processes was observed. In addition, the C_H2 domain unfolding was changed from a fully reversible transition in the IgG1 to be a partially reversible transition in case of ADC. The second transition representing the unfolding of the Fab is broadened (temperature width at half peak-height), indicative of the loosening of the structure and thus a less cooperative structural melt. The computed VdW volumes is in line with the picture of a looser structure for ADC. The major conjugation sites are located between heavy-light chains with a smaller portion of conjugation occurring between heavy-heavy chain disulfide bonds (data not shown). The decrease in the structural stability observed by DSC, for both the C_H2 domain and Fab after conjugation can thus be attributed to the cleavage of disulfide bonds and attachment of hydrophobic payload linker in these regions. From a high-order structure perspective, the similarity in secondary and tertiary structures between the parent mAb and ADC, but the lower thermal stability of the ADC suggests that the ADC has a less compact structure compared to the mAb. This agrees with the results from the DCVJ, Thioflavin T fluorescence spectroscopy, turbidity measurement and thermal incubation studies suggesting that the ADC is more prone to aggregation when compared to the mAb. Although both the first and second transitions could trigger the formation of oligomers in ADC, the second transition representing the unfolding of C_H3/Fab region is the major transition that leads to the formation of significant aggregates since only second transition is detected by Thioflavin T and also shows up as a sharp rise in turbidity.

In general, protein aggregation can arise from conformational instability as well as colloidal interactions (18,33,34). In the case of the ADC studied here, both of these sources of aggregation are present to a greater extent when compared with the parent mAb. The ADC possesses significantly lower conformational stability than its parent IgG1 mAb, and its molecular surface also becomes more hydrophobic thus reducing its colloidal stability. Consistent with the experimentally observed decrease in conformational destabilization (melting temperature, Cp and melt enthalpy), molecular modeling also indicates a substantial decrease in the potential energy of the mAb upon conjugation. Furthermore, the payload covers the polar regions on the mAb local surface making it more hydrophobic in the ADC thus resulting in colloidal destabilization. These insights generated show that the strategy for formulation of the ADC will need to address both the conformational (reduced structural stability) and colloidal (increased hydrophobicity) aspects. The DAR for cysteine conjugation can range from 2–8 (preferentially even numbers) (7), i. e. multiple DAR species are present in the drug substance pool after purification. Clearly, the higher the DAR, the greater the degree of destabilization and the more hydrophobic the species. It is therefore likely that these higher DAR species drive the instability of the overall pool and therefore these have to be the focus of the formulation efforts. Formulation would likely require presence of structure stabilizers such as sucrose (increase free energy of unfolding) in a low ionic strength solution (increase second virial coefficient) to provide stabilization against aggregation (35). The enhanced hydrophobicity will also make the ADC more susceptible to aggregation under interfacial stresses such as agitation and require the addition of surfactants to ameliorate this concern (36).

From a physical stability perspective, IgG1 mAb in this study is shown to be destabilized upon conjugation. Wakankar *et al.* also report that the conjugation of the drug moiety DM1 (mertansine) to trastuzumab results in destabilization of the C_H2 domain of the antibody (9). These observations raise the question whether conjugation of mAbs with small molecule drugs will always lead to ADCs with lower conformational stability and greater aggregation propensity compared to the parent. Although intuitively likely, evidence for such a general rule is insufficient at this point.

CONCLUSIONS

A systematic biophysical approach has been taken to better understand the impact of conjugation chemistry and the physico-chemical nature of the small molecule linkers and payloads on the higher order structure and therefore the physical stability of antibody-drug conjugates. The combination of computational and biophysical experimental techniques, including application of various fluorescence dyes, provides not only global insights but also local information into the structural stability and aggregation propensity of the antibody-drug conjugate. The experimental data and the computational models are in agreement with each other and show that although the secondary and tertiary structure of the mAb and ADC are similar, the conjugation of the hydrophobic payload destabilizes the ADC structure making it less compact and also more hydrophobic. These two changes (impacting the conformational and colloidal stability respectively) enhance the propensity of the ADC to form aggregates. This knowledge can be used to design the formulation to create a viable commercial drug product.

REFERENCES

1. Wu AM, Senter PD. Arming antibodies: prospects and challenges for immunoconjugates. Nat Biotechnol. 2005;23(9):1137–46.
2. Chari RV. Targeted cancer therapy: conferring specificity to cytotoxic drugs. Acc Chem Res. 2008;41(1):98–107.
3. Alley SC, Benjamin DR, Jeffrey SC, Okeley NM, Meyer DL, Sanderson RJ, *et al.* Contribution of linker stability to the activities

of anticancer immunoconjugates. Bioconjug Chem. 2008;19(3):759–65.
4. Baldwin AD, Kiick KL. Tunable degradation of maleimide-thiol adducts in reducing environments. Bioconjug Chem. 2011;22(10):1946–53.
5. Chih HW, Gikanga B, Yang Y, Zhang B. Identification of amino acid residues responsible for the release of free drug from an antibody-drug conjugate utilizing lysine-succinimidyl ester chemistry. J Pharm Sci. 2011;100(7):2518–25.
6. Hamblett KJ, Senter PD, Chace DF, Sun MM, Lenox J, Cerveny CG, *et al.* Effects of drug loading on the antitumor activity of a monoclonal antibody drug conjugate. Clin Cancer Res Off J Am Assoc Cancer Res. 2004;10(20):7063–70.
7. Sun MM, Beam KS, Cerveny CG, Hamblett KJ, Blackmore RS, Torgov MY, *et al.* Reduction-alkylation strategies for the modification of specific monoclonal antibody disulfides. Bioconjug Chem. 2005;16(5):1282–90.
8. Wakankar A, Chen Y, Gokarn Y, Jacobson FS. Analytical methods for physicochemical characterization of antibody drug conjugates. mAbs. 2011;3(2):161–72.
9. Wakankar AA, Feeney MB, Rivera J, Chen Y, Kim M, Sharma VK, *et al.* Physicochemical stability of the antibody-drug conjugate Trastuzumab-DM1: changes due to modification and conjugation processes. Bioconjug Chem. 2010;21(9):1588–95.
10. Hu L, Olsen C, Maddux N, Joshi SB, Volkin DB, Middaugh CR. Investigation of protein conformational stability employing a multimodal spectrometer. Anal Chem. 2011;83(24):9399–405.
11. Fan H, Ralston J, Dibiase M, Faulkner E, Middaugh CR. Solution behavior of IFN-beta-1a: an empirical phase diagram based approach. J Pharm Sci. 2005;94(9):1893–911.
12. Kayser V, Chennamsetty N, Voynov V, Helk B, Trout BL. Conformational stability and aggregation of therapeutic monoclonal antibodies studied with ANS and Thioflavin T binding. mAbs. 2011;3(4):408–11.
13. Ramsey JD, Gill ML, Kamerzell TJ, Price ES, Joshi SB, Bishop SM, *et al.* Using empirical phase diagrams to understand the role of intramolecular dynamics in immunoglobulin G stability. J Pharm Sci. 2009;98(7):2432–47.
14. Guo J, Harn N, Robbins A, Dougherty R, Middaugh CR. Stability of helix-rich proteins at high concentrations. Biochemistry. 2006;45(28):8686–96.
15. Saphire EO, Parren PW, Pantophlet R, Zwick MB, Morris GM, Rudd PM, *et al.* Crystal structure of a neutralizing human IGG against HIV-1: a template for vaccine design. Science. 2001;293(5532):1155–9.
16. Berman HM, Westbrook J, Feng Z, Gilliland G, Bhat TN, Weissig H, *et al.* The Protein Data Bank. Nucleic Acids Res. 2000;28(1):235–42.
17. Franey H, Brych SR, Kolvenbach CG, Rajan RS. Increased aggregation propensity of IgG2 subclass over IgG1: role of conformational changes and covalent character in isolated aggregates. Protein Sci Publ Protein Soc. 2010;19(9):1601–15.
18. Agrawal NJ, Kumar S, Wang X, Helk B, Singh SK, Trout BL. Aggregation in protein-based biotherapeutics: computational studies and tools to identify aggregation-prone regions. J Pharm Sci. 2011;100(12):5081–95.
19. Sreerama N, Manning MC, Powers ME, Zhang JX, Goldenberg DP, Woody RW. Tyrosine, phenylalanine, and disulfide contributions to the circular dichroism of proteins: circular dichroism spectra of wild-type and mutant bovine pancreatic trypsin inhibitor. Biochemistry. 1999;38(33):10814–22.
20. Kueltzo LA, Ersoy B, Ralston JP, Middaugh CR. Derivative absorbance spectroscopy and protein phase diagrams as tools for comprehensive protein characterization: a bGCSF case study. J Pharm Sci. 2003;92(9):1805–20.
21. Nonoyama A, Laurence JS, Garriques L, Qi H, Le T, Middaugh CR. A biophysical characterization of the peptide drug pramlintide (AC137) using empirical phase diagrams. J Pharm Sci. 2008;97(7):2552–67.
22. He F, Hogan S, Latypov RF, Narhi LO, Razinkov VI. High throughput thermostability screening of monoclonal antibody formulations. J Pharm Sci. 2010;99(4):1707–20.
23. Haidekker MA, Brady TP, Lichlyter D, Theodorakis EA. Effects of solvent polarity and solvent viscosity on the fluorescent properties of molecular rotors and related probes. Bioorg Chem. 2005;33(6):415–25.
24. Haidekker MA, Theodorakis EA. Environment-sensitive behavior of fluorescent molecular rotors. J Biol Eng. 2010;4:11.
25. Hawe A, Filipe V, Jiskoot W. Fluorescent molecular rotors as dyes to characterize polysorbate-containing IgG formulations. Pharm Res. 2010;27(2):314–26.
26. Kung CE, Reed JK. Fluorescent molecular rotors: a new class of probes for tubulin structure and assembly. Biochemistry. 1989;28(16):6678–86.
27. Lindgren M, Sorgjerd K, Hammarstrom P. Detection and characterization of aggregates, prefibrillar amyloidogenic oligomers, and protofibrils using fluorescence spectroscopy. Biophys J. 2005;88(6):4200–12.
28. Nelson R, Sawaya MR, Balbirnie M, Madsen AO, Riekel C, Grothe R, *et al.* Structure of the cross-beta spine of amyloid-like fibrils. Nature. 2005;435(7043):773–8.
29. Sawaya MR, Sambashivan S, Nelson R, Ivanova MI, Sievers SA, Apostol MI, *et al.* Atomic structures of amyloid cross-beta spines reveal varied steric zippers. Nature. 2007;447(7143):453–7.
30. Brummitt RK, Nesta DP, Chang L, Kroetsch AM, Roberts CJ. Nonnative aggregation of an IgG1 antibody in acidic conditions, part 2: nucleation and growth kinetics with competing growth mechanisms. J Pharm Sci. 2011;100(6):2104–19.
31. Mason BD, Zhang L, Remmele Jr RL, Zhang J. Opalescence of an IgG2 monoclonal antibody solution as it relates to liquid-liquid phase separation. J Pharm Sci. 2011;100(11):4587–96.
32. Ionescu RM, Vlasak J, Price C, Kirchmeier M. Contribution of variable domains to the stability of humanized IgG1 monoclonal antibodies. J Pharm Sci. 2008;97(4):1414–26.
33. Buck PM, Kumar S, Wang X, Agrawal NJ, Trout BL, Singh SK. Computational methods to predict therapeutic protein aggregation. Methods Mol Biol. 2012;899:425–51.
34. Sahin E, Grillo AO, Perkins MD, Roberts CJ. Comparative effects of pH and ionic strength on protein-protein interactions, unfolding, and aggregation for IgG1 antibodies. J Pharm Sci. 2010;99(12):4830–48.
35. Chi EY, Krishnan S, Randolph TW, Carpenter JF. Physical stability of proteins in aqueous solution: mechanism and driving forces in nonnative protein aggregation. Pharm Res. 2003;20(9):1325–36.
36. Lee HJ, McAuley A, Schilke KF, McGuire J. Molecular origins of surfactant-mediated stabilization of protein drugs. Adv Drug Deliv Rev. 2011;63(13):1160–71.